Investigation of Far-Infrared Emission Characteristics of Graphene Health Belt with Near-Infrared LED Embedded in LED Module/Carbon Nanographene Fabric PPMatrix for Health and Medical Devices

Dong-Myong Kim[1,2*,] Hyung-Kon Lee[1], Yong-Seong Kwon[1,2], Yeon-Mea Choi[2],GreethiLavi[3], Abdul Kahid[3], Dae-Hyun Kim[3]

[1]*R&D Center of KJMbio Co. Ltd, Seoul, Korea*
[2]*KimJeongMoon Aloe Ltd., Seoul, Korea*
[3]*Nano Process & Device Laboratory of Hanyang University,Seoul, Korea*
*Corresponding Author

ABSTRACT: *Far infrared (FIR) radiation within the wavelength range of 4–14 µm can provide human health benefits such as improved blood flow. Therefore, in this study, a belt that can effectively promote health by emitting far infrared (FIR) radiation via near infrared (NIR) radiation was developed by fusing LED module/carbon nanographene fabric matrix. In this study, the potential of LED module/carbon nanographene fabric matrix as a health promotion belt was investigated. The properties of LED module/carbon nanographene fabric polypropylene (PP) matrix (LED/G-FM; BIOC^{TM}) were compared with other far infrared (FIR) emitting matrices such as hematite, rust, and graphene. With the application of BIOC, the FIR emittance increased to 0.90, which was 9% higher than that of the pristine graphene fabric matrix. In addition, BIOC achieved a UV blocking super protection factor (UPF) of 91.41 and a NIR emittance of 95.85% by enhancing the UV blocking and NIR and FIR enhancement functions. In addition, the result of incorporating 2 wt% BIOC showed improved heat retention, showing 3.3 times higher temperature rise than pure graphene fabric PP matrix after 30 seconds of exposure to FIR source. In addition, the ability to achieve the lowest thermal efficiency among other fabric matrices supports the potential use of BIOC hybrid belts as health and medical devices. The tensile properties of belts with BIOC are superior to other fabric matrices, which may contribute to extending product life and convenience.*

KEYWORDS *far-infrared, carbon nanographene, near-infrared radiation, LED module, fabric polypropylene matrix, health belt, emission characteristics,thermal effect, medical devices.*

Date of Submission: 02-11-2024   Date of acceptance: 12-11-2024

I. INTRODUCTION

Far infrared (FIR) radiation falls within the electromagnetic spectrum of 750–1000 µm. Objects above absolute zero, such as the human body at room temperature, emit FIR. This radiation is perceived as radiant heat by human thermoreceptors. The human body effectively absorbs FIR due to its high-water content, causing molecules in the body to undergo various vibrational motions [1]. FIR radiation in the range of 4–14 µm, also known as "life rays," can penetrate human skin and generate heat through resonance effects caused by microscopic vibrations within molecules [2]. This resonance process can promote cell function by dilating capillaries and improving blood circulation [3].

Furthermore, studies have shown that FIR can enhance the viability of cells and tissues, decrease the sensitivity of neuroblastoma cells to rotenone (an inhibitor of mitochondrial respiration), and alleviate mitochondrial fragmentation. This, in turn, helps prevent the onset of Spinocerebellar ataxia type 3, which is associated with neurodegenerative dis- eases [4].

In recent years, researchers have conducted human trials using fabrics incorporating near-infrared emitting matrices to explore the health benefits of applying FIR. For example, bed sheets incorporating near-

infrared emitting bioceramics were shown to alleviate insomnia symptoms and reduce daytime sleepiness in a randomized controlled trial of 29 adults. This effect may be attributed to nitric oxide (NO)-induced vasodilation, potentially increasing perfusion and skin temperature [5]. Another study of 12 physically active male cyclists showed that oxygen consumption during low-intensity exercise was reduced when participants wore clothing incorporating far-infrared emitting ceramics compared to standard clothing. It has been suggested that the ceramics promote the release of NO, leading to vasodilation and improved oxygenation to muscles during low-intensity cycling [6]. Infrared radiation can also be caused by changes in dipole moment due to molecular vibration [7]. For example, tourmaline exhibits high FIR emission even at low temperatures due to its atomic arrangement. However, a slight temperature change can modify the dipole moment of molecules in the material, which can increase molecular excitation and thus increase infrared radiation emission [8]. Previous studies [9] have also shown that iron oxide-based natural mineral additives have excellent FIR emission due to molecular vibrations at FIR wavelengths. According to Kirchhoff's emission law, absorption at FIR wavelengths is equal to emission at thermal equilibrium at the same wavelength.

Besides inorganic fillers, carbon nanostructures such as graphene have also shown promising far-infrared emittance due to the presence of π-electron optical transitions [10]. Zhao et al. [11] synthesized graphene/MnO_2 composites via hydrothermal method and reported that they exhibited higher FIR emittance than pure MnO_2. The reason for this enhanced FIR emittance is that the number of molecules on the exposed surface increases, resulting in a larger specific area, which in turn increases the surface energy. In addition to the enhanced FIR emittance, graphene and natural mineral additives such as hematite also possess other functional properties such as UV blocking [12,13] and excellent thermal conductivity [14,15].

Despite these functional properties, both hematite and graphene show poor compatibility with nonpolar polymers such as polypropylene to form strong polymer/filler interfaces. Although reduction of graphene oxide to graphene is expected to remove all functional groups, obtaining 100% pure graphene is still challenging, and polar functional groups such as carboxylic acids are often present. Furthermore, obtaining high-purity graphene is expensive, and concentrations exceeding 0.5 wt% should be used cautiously, especially if not incorporated into smart fibers that utilize its superior electrical properties. Hematite, a polar compound, has been shown to improve mechanical and wettability properties when added to polar polymers such as polyurethane [16].

To improve the compatibility of nonpolar polymers and polar matrices, various methods have been proposed, including the addition of compatibilizers such as maleic anhydride graft polymers [17], the utilization of coupling agents such as silanes [18] to promote surface compatibility, and in situ polymerization [19]. However, these techniques have drawbacks, including increased cost. In situ polymerization is limited to low viscosity polymers to ensure effective reaction [20]. In addition, it is important to optimize the amount of coupling agents and compatibilizers. Excessive use of these chemicals can cause plasticization effects, which can reduce stiffness, hardness [21], and strength [22]. Therefore, there is a need to develop matrices that can be chemically modified using simple methods without the need for nonpolar groups or expensive chemicals.

LED module/carbon nanographene fabric polypropylene (PP) matrix (LED/G-FM; BIOC™)has drawn attention for many years since our laboratory examined the near-infrared emission effects of LED modules and far-infrared emission of carbon nanographene fibers, and a patented technology to support its sustainability has been filed [23,24]. In addition, the low density of BIOCmakes it particularly suitable for lightweight matrix applications such as fiber manufacturing [24,25]. One of the most attractive features of BIOC is its tunable functionality depending on the pyrolysis temperature. A study conducted by Kim et al. [23] investigated the possibility of configuring fabric matrices with various LED modules and carbon nanographene and the effect of pyrolysis temperature on the LED module-carbon nanographene interaction. The results showed that when BIOCwas pyrolyzed at temperatures below 40°C, the near-infrared emission by the LED module was significantly enhanced compared to the far-infrared emission of carbon nanographene. This suggests that these BIOCcan increase far-infrared emissions relative to near-infrared radiation [23].

Therefore, we are interested in investigating the FIR emissivity and thermal efficiency of the BIOCfusion composites, which have not been attempted before, by fusing highly active BIOC at low pyrolysis temperature similar to body temperature. Although the UV blocking properties of carbon nanographene-based coated fibers have been studied [23, 26-28], their UV blocking capabilities for textile applications have not been explored. Therefore, in this study, we attempted to utilize the BIOCfusion technique to remove polar functional groups even at low pyrolysis temperature. The resulting pyrolytic BIOCwas investigated to investigate its effect on FIR emissivity, UV blocking, and thermal efficiency. Matrices containing graphene and iron-based minerals such as hematite and indocyanine were also studied for comparison.

This study demonstrates that BIOCcan significantly increase FIR and NIR emittance, enhance UV blocking, improve heat retention, and maintain superior tensile properties compared to other metrics. The significance of this study is to advance the development of IR-emitting materials for potential future applications of BIOC, providing potential health and disease treatment benefits and improved thermal comfort.

II. RESEARCH METHODS

A. Preparationof FIR-emitting BIOCandFunctionalMaterials

To obtain BIOC, LEDs were purchased from Tencan Co. (GJ-1, Changsha, China) and assembled into LED modules by KJMBio Co. (Seoul, Korea) as shown in Fig. 1. Carbon nanographene was purchased from Angstron Materials Inc. (Ohio, USA) and carbon nanographene fabric was manufactured by HNC Co. (Yongin, Korea) to fabricate LED/G-FM matrix (Fig. 2). In our previous study, we showed that when PP was fused with BIOC and connected to a rechargeable battery (10,000 mAh/3.7 V, input-output 5V-2A, Shenzen KIDD Thenol. Co., China) and a power source, the carbon nanographene-coated PP emitted more NIR and FIR [23].

Hematite (HEM) was purchased from Mikon Co. (Singapore) and ground into powder using a fine powder grinder (Chungching MP-M, Chongqing, China) and then sieved through a 10 µm sieve before use. Red ochre (ROCH) was purchased from Konstantas (https://konstantas.com/, accessed on June 1, 2024). 96% purity graphene (GN) and PP was purchased from Sigma-Aldrich, St. Louis, Missouri, USA.
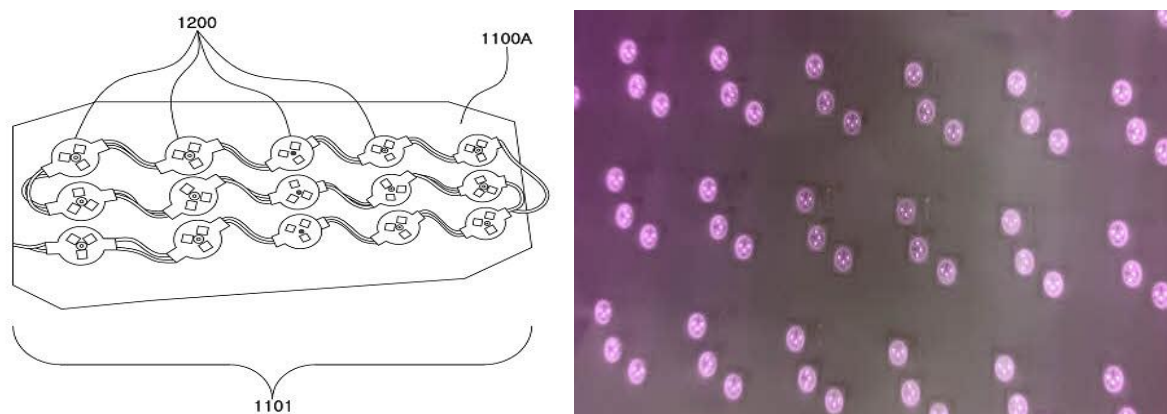

Fig.1. BIOCDiagram showing the near-infrared LED modules inside the matrix (left) and a photographic image of the light emitted by the near-infrared LED (right)
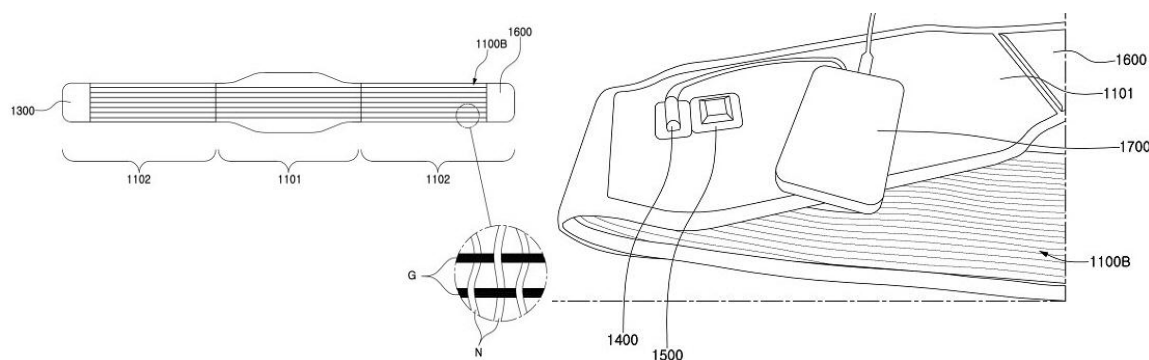

Fig.2. BIOC diagram showing a graphene health belt with near-infrared LEDs embedded with carbon nanographene fibers, combined with a portable battery and PP film (right)

B. Manufacturing of PP Composite Films

BIOC, HEM and ROCH were blended with PP (LyondellBasell, Netherlands) at 0.5 wt% and 2 wt%, respectively, using a laboratory-scale twin-screw extruder (Wuhan Ruiming, China) at 180°C with controlled rotation speed. The temperatures of the feed zone, compression zone and melting zone were set at 120°C, 170°C and 180°C, respectively. The rationale for these settings was to preheat the material in the feed zone, gradually melt it in the compression zone and finally ensure that the plastic is uniformly melted in the extruder. The extruded filaments were air-dried and pelletized. The pellets were then hot-pressed at 180°C for 10 min using a square mold measuring 150 x 150 x 0.5 mm. Blank samples (PP BLK) with only PP as the sample amount and samples with 0.5 wt% GN were also extruded under the same conditions and molded using a hot press to serve as controls for comparison. The reason we used only 0.5 wt% graphene is because it is expensive, not economical at higher concentrations, and tends to agglomerate at higher concentrations.

C. Characterization of UV blocking and NIR enhancement of matrix

The UV radiation spectrum from 290 to 400 nm and the NIR radiation spectrum from 780 to 2500 nm of PP film containing matrix were obtained using a UV-VIS NIR spectrometer (Agilent Cary 60 UV-Vis spectrometer, Cary, NC, USA) and the average of three samples was calculated. The UV blocking properties were analyzed using the method of AS/NZS 4399:1 996 standard [29]. The arithmetic mean of UVA transmittance (UVA$_{AV}$), UVB transmittance (UVB$_{AV}$), UV radiation (UVR$_{AV}$), and ultraviolet protection factor (UPF) were calculated according to the following formulas:

(1) UVA$_{AV}$ (%) = $T_{315} + T_{320} \ldots \ldots .. T_{395} + T_{400}$ / 18
(2) UVB$_{AV}$ (%) = $T_{290} + T_{295} \ldots \ldots .. T_{310} + T_{315}$ / 6
(3) UVR$_{AV}$ (%) = $T_{290} + T_{295} \ldots \ldots .. T_{395} + T_{400}$ / 23
(4) UPF = $\sum_{290}^{400} E(\lambda) \times S(\lambda) \times \Delta\lambda$ / $\sum_{290}^{400} E(\lambda) \times S(\lambda) \times \Delta\lambda$

Where $T(\lambda)$ is the percentage spectral transmittance of the sample at wavelength λ, $E(\lambda)$ is the relative erythema spectral effect, $S(\lambda)$ is the solar spectral irradiance in W m^{-2}·nm^{-1}, and $\Delta\lambda$ is the measured wavelength interval in nm. The UPF protection category is adopted from the AS/NZS 4399:1 996 standard.

The NIR emittance of blank PP films with matrix was calculated by comparing the area under the curve (AUC) of the transmittance spectrum with 100% transmittance, using the following formula :

(5) NIR emittance (%) = (1 –*AUC of samples at 780–2500 nm / AUC of spectra with 100% transmittance at 780–2500 nm*)

D. Thermal Analysis and Heat Storage Characterization

The thermal properties of PP composites were characterized using a Q10 DSC (TA Instruments, New Castle, DE, USA) using the heating-cooling-heating method according to the ISO 11357-1:2023 standard [30] and the average curve of three samples is reported. Briefly, approximately 5 mg film samples were heated from 30 to 50 °C at a rate of 10 °C/min and then cooled to 30 °C at the same cooling rate of 10 °C/min. The samples were reheated using the same conditions used during the first heating cycle. The melting temperature (Tm), crystallization temperature (Tc), and heat of fusion (ΔHm) of the samples were then obtained and analyzed during the second heating process. The degree of crystallinity (Xc) was calculated using the following formula:

(6)$X_C = \Delta Hm$ / $\Delta Hm_{100} (1 - w_f)$

where, ΔHm is the heat of fusion of the sample. $\Delta Hm100$ is the heat of fusion of 100% PP, which is 204 J/g [31]. W_f is the weight fraction of the matrix.

Given the normality assumption behind the *p*-value calculation of the regression coefficients, filament width and roughness were log transformed before fitting the regression models. Ordinary least square regression (OLS) with Akaike information criterion (AIC)-based stepwise model selection was used to determine which interaction terms to include in the regression model.

D. Other characterizations

Raman spectroscopy was performed with a WITEC Confocal Raman (Oxford instruments, Oxford, UK) with a laser wavelength of 488 nm. A 20x objective was used and scanning was performed from -2000 cm^{-1} to 3000 cm^{-1}. Cross sections of PP composite films were obtained after cryogenic fracture with liquid nitrogen. The fracture surfaces of PVC composites were coated with gold using a sputter coater and observed with a field emission scanning electron microscope (FE-SEM) (JEOL 7600F, Japan) at 5 kV. Fourier transform infrared spectroscopy was performed at GN and BIOC. Powder samples were pelletized with KBr and analyzed by 16 scans through a slide holder with a 1 cm diameter hole and a FTIR spectrometer (Perkin Elmer Frontier, USA) with a resolution of 4 cm^{-1}. The emissivity of the films in the wavelength range of 4–15 μm was measured using a Far Infrared Emissivity Analysis System (HOTECH EMS302M, Taiwan) at 34°C.

Emissivity measurements of the films were referenced to a value of 1, which is that of a perfect black body, emitting all possible thermal radiation at a given temperature, whereas 0 represents a perfect reflector, emitting no thermal radiation. The thermal efficiency of the PP films was obtained at 2 and 10 seconds at a temperature of 24 °C using a thermal efficiency meter (Thermtest, Hanwell, NB, Canada).

ANCOVA was performed to analyze the release rate results and ANOVA was used for the runoff rate results. Both were performed using the DATAtab statistical online calculator (https://datatab.net/, accessed September 14, 2024). In the ANCOVA analysis, the release rate was the dependent variable and the sample

acted as a covariate. For the ANOVA analysis on the runoff rate, the runoff rate was treated as a quantitative variable and the sample was a nominal variable.

Tensile tests were performed using an MTS Criterion Model 43 (Criterion, New York, NY, USA). Five film strips were tested with a width of 1.5 cm and a grip spacing of 10 cm according to the ASTM D882 standard [32]. The test speed used was 12.5 mm/min.

III. RESULTS AND DISCUSSION

A. Raman and FTIR spectra of carbon nanographene and BIOC

Raman spectroscopy was performed on both BIOC and GN to analyze the presence of defects and graphitization in the carbon-based materials. As shown in Fig.3a, the peak at 1330 cm^{-1} for both materials are attributed to the D band, indicating the presence of defects in the crystal lattice that destroy the hexagonal carbon structure [33,34]. The peak at around 1600 cm^{-1} is assigned to the G band, indicating highly ordered graphitic carbon [35]. In addition, the peak at around 2697 cm^{-1} is associated with the 2D band, which is used to distinguish the number of layers in the carbon structure. For GN, a sharp peak was observed, indicating a typical single-layer structure of graphene. In contrast, the 2D peak for BIOC is broad, indicating a multilayer carbon structure [36].

The ID/IG ratio, which is the ratio of the intensity of the D band to the intensity of the G band, is used to determine the degree of graphitization of carbon materials. A lower ID/IG ratio indicates a higher degree of graphitization. As shown in Figure 1a, the ID/IG ratio of GN is low, suggesting a very high degree of graphitization and a low number of defects. However, the ID/IG ratio of 0.87 for BIOC is lower than those reported for BIOC from other sources, indicating that composites containing BIOC may have improved mechanical properties [23,31,37].
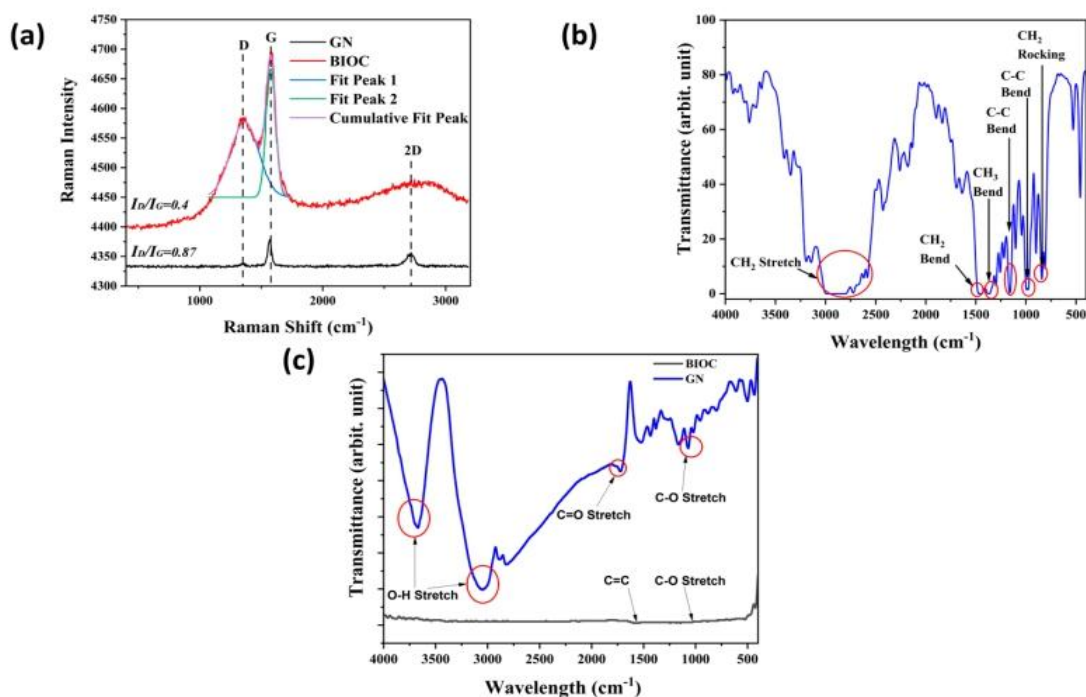

Fig.3. (a) Raman spectra of GN and BIOC from 400 cm^{-1} to 3000 cm^{-1}; (b) FTIR spectrum of pure PP from 4000 cm^{-1}–400 cm^{-1}; (c) FTIR spectra of GN and BIOC from 4000 cm^{-1}–400 cm^{-1}

The polarity was evaluated by identifying the functional groups present in the carbon-based powder and blank PP film using FTIR. The FTIR spectrum of the original PP film is shown in Fig. 3b. The peak at 2896 cm^{-1} corresponds to CH$_2$ asymmetric stretching. The peaks at 2724 cm^{-1}, 2619 cm^{-1}, and 2582 cm^{-1} correspond to CH$_2$ symmetric stretching. The peak at 1455 cm^{-1} corresponds to CH$_2$ symmetric bending. The peak at 1370 cm^{-1} corresponds to the symmetric bending vibration mode of CH$_3$ groups [38]. The peak at 1161 cm^{-1} corresponds to the C-C bending, which is the backbone of PP [39]. The peak at 994 cm^{-1} corresponds to CH$_3$ asymmetric rocking. The peak at 841 cm^{-1} corresponds to CH$_2$ rocking vibration [40] These results are consistent with the chemical structure of PVC, which contains only hydrocarbons and is nonpolar. Fig. 3c shows the IR spectra of GN and BIOC. In the spectrum of GN, the peaks at 3670 cm^{-1} and 3050 cm^{-1} correspond to the O–H group stretching vibration. The peak at 1722 cm^{-1} is assigned to the C=O stretching of carboxylic acids.

The peak at 1022 cm^{-1} is assigned to the C–O stretching vibration [41]. In the spectrum of BIOC, the peak at 1569 cm^{-1} is related to the presence of C=C bonds associated with the conjugation of π electrons and the presence of cyclic alkenes [42]. The peak at 1156 cm^{-1} is due to the C–O stretching vibration in alcohols [43].

B. Far-infrared emissivity of PP films with functional carbon nanographene

The far-infrared emissivity of PP films with 0.5 and 2 wt% carbon nanographene at 4–15 µm is shown in Fig. 4 for blackbody radiation. The film samples with carbon nanographene were studied by SEM by implementing a mapping function to confirm the presence of carbon nanographene in the film and to determine the particle distribution in the matrix. The SEM study results are shown in Fig. 5. Overall, all samples with carbon nanographene showed higher emissivity compared to the PP blank film. The variation in emissivity results is significant since $p < 0.001$ using ANCOVA (see Figure S5). In particular, the PP film with 2 wt% ROCH achieved the highest emissivity of 0.97. ROCH, which is mainly composed of iron oxide, exhibits various phonon modes associated with the vibrations of Fe and O atoms. Thermal energy excites these phonons to emit far-infrared radiation [44]. In contrast, the film with the lowest emissivity measured after adding carbon nanographene was 0.87 for 0.5 wt% HEM. Interestingly, the PP film with 0.5 wt% GN achieved an emissivity of 0.96, which is consistent with the results of Hu et al. [45], who showed that a small amount of graphene coating on polyurethane can significantly enhance the far infrared emissivity of the resulting composite. The high emissivity of graphene can be attributed to the presence of π electron optical transitions, which enhances absorption and emission in the infrared region [10].
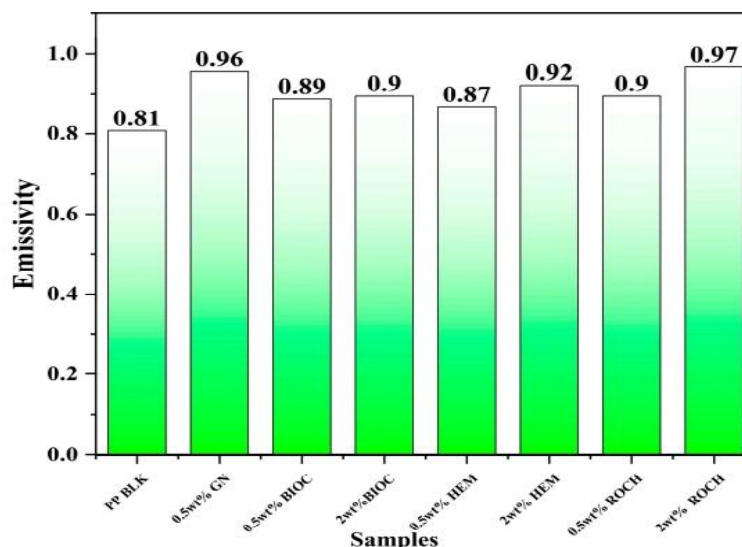

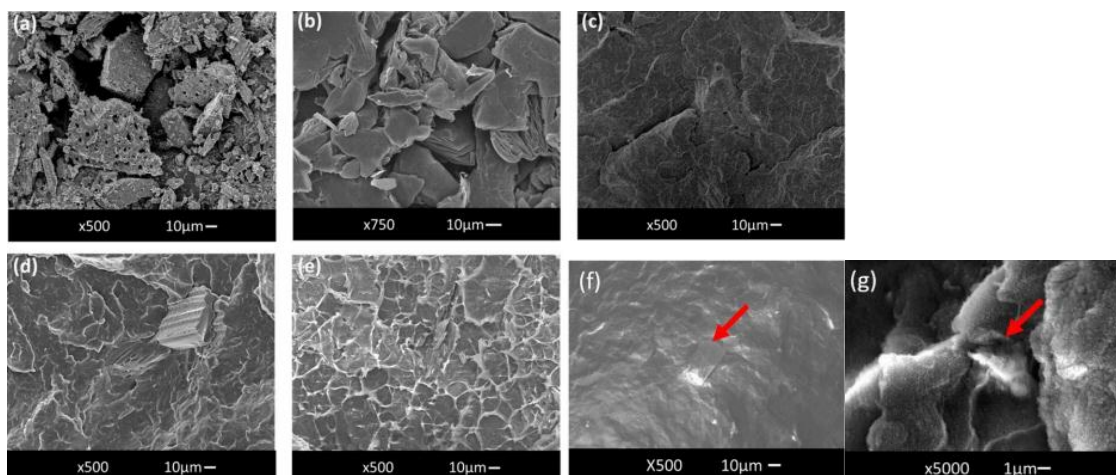**Fig.4. FIR emissivity at 5–14 µm of the PP films with 0.5% and 2% additives**

Fig.5. SEM images of (a) BIOC, (b) graphene, (c) neat PP, (d) PP + 2 wt% BIOC, (e) PP + 0.5 wt% GN, (f) PP + 2% HEM (red arrows point to the HEM particles), and (g) PP + 2% ROCH. (Red arrows indicate the positions of ROCH particles)

When the carbon anodic graphene concentration increased from 0.5 wt% to 2 wt%, the emissivity of the films also increased, from +0.8% for the PP film with BIOC to +8% for the PP film with ROCH. Although the emissivity was lower than that of the PP films with GN, ROCH, and HEM, the PP film with BIOC showed a significant increase in emissivity up to +10.8% at 2 wt%. This enhancement can be attributed to the porous structure of the BIOC(as observed in Fig. 5a), where higher porosity provides a larger surface area for the absorption and reflection of electromagnetic waves, thereby resulting in higher emissivity [46].

Materials with higher emissivity can efficiently convert sunlight or human body thermal energy into electromagnetic radiation. The emissivity of a perfect heat emitter, known as a black body, is 1. Therefore, despite its lower emissivity than other additives, PP with 2 wt% BIOC achieved an emissivity of 0.90 for black body radiation, which is higher than the far-infrared emissivity of ceramic-embedded polymers reported previously [47]. The emissivity of 0.9 indicates that PP with 2 wt% BIOC can emit 90% of black body radiation within 4–15 μm, whereas pure PP emits only 81% of black body radiation. Increasing the BIOC concentration from 0.5 wt% to 2 wt% only increases the emissivity by 0.01, suggesting that there is a saturation limit for the emissivity effect with BIOC concentration. This may be due to the relatively higher tendency of BIOC to aggregate at 2 wt% compared to 0.5 wt%.

C. Thermal release and heat retention properties of PP films with functional matrices

Thermal release is defined as the ability of a material to transfer thermal energy to its surroundings and is directly proportional to the thermal conductivity of the material [48]. Since the thermal conductivities of HEM, ROCH, and GN are higher than those of PP, it is expected that their thermal release will increase after incorporation into PP, as shown in Fig. 6a. However, all samples with functional matrices incorporated generally have lower thermal release than pure PP. Since $p < 0.001$, the null hypothesis is rejected, indicating that the variance of release is statistically significant (see Fig. S6). The thermal release further decreases as the matrix concentration increases from 0.5 wt% to 2 wt%. The decrease in thermal efficiency of samples with HEM, ROCH, and GN incorporated may be due to the poor interaction at the interface between the matrix and PP (see Fig. 5e–g). This inhibits the heat transfer between the composites, resulting in lower thermal efficiency [49,50]. The poor filler/matrix interface when adding GN is shown in Fig. 5e.

The lowest thermal effusively is observed in PP films with 2 wt% BIOC, with a value of 413.23 W$\sqrt{}$ s/m^2 K at 10 s. This low thermal effusively from PP film incorporated with BIOC is attributed to the high porosity of biochar, as shown in Figure 5d. Bordoloi et al. [51] reported that the heat transfer of material was hindered after biochar was added into an organic phase change material due to the high porosity of biochar, which may introduce heat-resistant air voids. A material with higher thermal effusively provides the wearer with a colder sensation, while a material with lower thermal effusively gives the wearer a warmer feel. These results suggest that BIOC can potentially be used as an additive to textiles, providing a warming effect.

A lamp test was conducted following a previous study, where samples were exposed to an IR lamp and then cooled to observe the heat retention capabilities of the composites [23, 52]. However, the testing time was adjusted to 30 s as the polymer samples were thinner compared to the fabrics reported in the previous study. Figure 6b illustrates the temperature difference of the PP films after exposure to the IR lamp for 30 s and subsequent cooling for 30 s after the IR lamp was switched off. The results indicated that all PP films with additives at both 0.5 and 2 wt% exhibited better heat retention capabilities than pristine PP. With an increase in the concentration of additives, the temperature increment upon exposure to the IR lamp was also enhanced. Films with 2 wt% BIOC achieved the highest temperature increase of +36.45 ℃. Both films with HEM and ROCH had a lower temperature increment compared to the film with the carbon-based additives, with an increase of +25.97℃ and +17.84 ℃ at 2 wt%, respectively. Even after 30 s when the IR lamp was switched off, all films with additives displayed a higher net increase in temperature ranging from +11.39℃ to +28.86 ℃ compared to pristine PP, which showed a net increase of only +6.89 ℃.

The basis for the higher temperature increases after IR lamp exposure may be due to the higher ability of GN and BIOC to absorb far-infrared radiation. According to the study of Mak et al. [53], graphene exhibits excellent far-infrared absorption due to intraband transitions at low phonon energies. The high temperature increase of BIOC may be due to its low outflow due to its porous structure. Materials with low outflow also have low thermal conductivity, which means that no heat is lost to the surroundings, which accelerates the temperature increase when exposed to a radiation source [54].
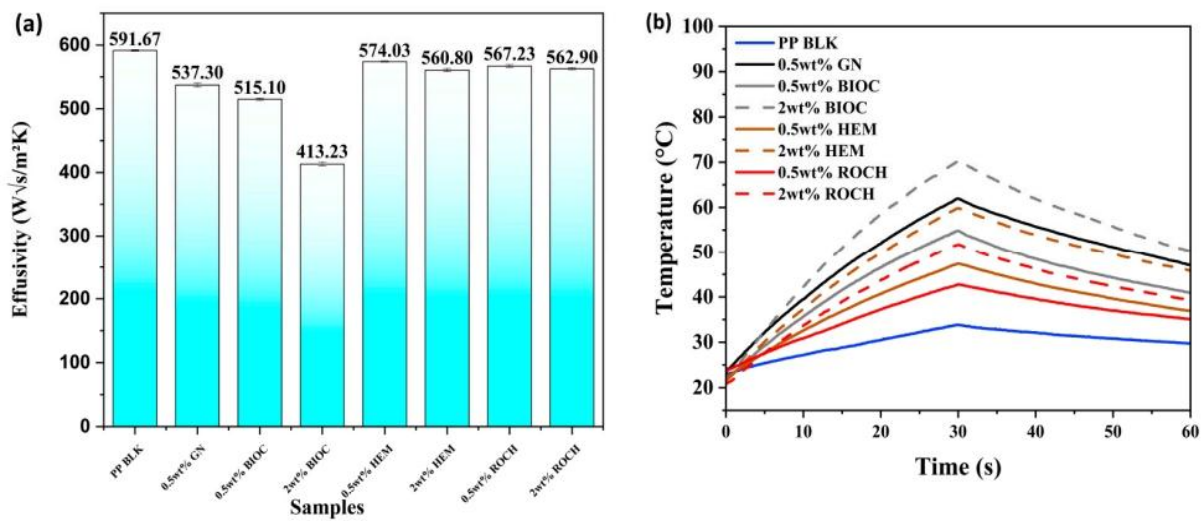
Fig.6. Thermal properties of matrix-added PP films: (a) Heat release rate of PP films with 0.5 wt% and 2 wt% matrix at 10 s contact time; (b) Heat retention of PP films with additives showing temperature difference change from initial temperature of films with 0.5 wt% and 2 wt% matrix after irradiating with infrared for 30 s (0–30 s) and after turning off the infrared irradiation (30–60 s)

D. Thermal properties by DSC analysis

Thermometry of DSC analysis is shown in Fig. 7. The melting endotherm of PP samples with matrix is summarized in Table 1. In general, the melting temperature did not change compared to pure PP even with the addition of up to 2 wt% matrix, suggesting that the melting behavior of the composites is similar to that of typical PP. However, the addition of GN, BIOC, HEM, and ROCH increased the melting energy and crystallinity of PP. The increase in melting energy with the addition of these additives is due to the incorporation of thermally stable additives into the PP matrix [55]. The addition of these matrices also increases the crystallinity, which promotes the formation of spheres and enhances the crystallization process [56]. The crystallinity further improves with increasing matrix concentration. PP with 2 wt% HEM showed the highest melting energy and crystallinity, while PP with 0.5 wt% showed the lowest. Although various studies have reported that the addition of these matrices does not affect the crystallization temperature, our results contradict this notion. Instead, the results of this study indicate that the addition of a matrix other than PP containing 0.5 wt% HEM does not affect the crystallization temperature. This discrepancy may be due to the lower concentrations used in this study, which may not be sufficient to promote crystallization, whereas the concentrations used in previous studies were typically at least 10 wt%.
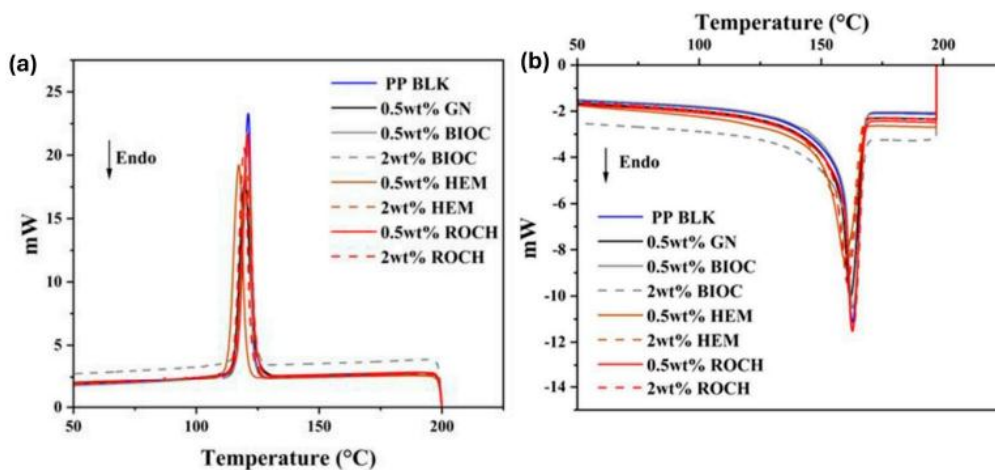

Fig.7. DSC thermograms of PP films with matrix: (a) cooling thermogram from 200 °C to 30 °C; (b) second heating thermogram from 30 °C to 200 °C

Table 1. DSC melting temperature (Tm), crystallization temperature (Tc), and degree of crystallinity (Xc) of PVC films and their standard deviations (including 0.5 and 2 wt% matrix)

Films	Tm (°C)	Tc (°C)	ΔH_m (J/g)	X_c (%)
PP BLK	162.79 ± 0.01	120.85 ± 0.25	77.88 ± 0.33	37.26 ± 0.16
0.5 wt% GN	161.76 ± 0.17	119.77 ± 0.02	88.89 ± 1.30	44.77 ± 0.65
0.5 wt% BIOC	162.92 ± 0.11	120.79 ± 0.09	87.51 ± 0.48	42.08 ± 0.23
2 wt BIOC	163.29 ± 0.16	120.87 ± 0.18	88.88 ± 0.58	43.39 ± 0.29
0.5 wt% HEM	159.69 ± 0.08	117.64 ± 0.35	86.58 ± 1.92	41.63 ± 0.92
2 wt% HEM	160.87 ± 0.30	120.46 ± 0.23	95.25 ± 0.75	46.50 ± 0.37
0.5 wt% ROCH	160.48 ± 1.54	121.12 ± 0.15	76.14 ± 0.85	36.61 ± 0.41
2 wt% ROCH	160.72 ± 0.11	119.36 ± 0.04	81.46 ± 2.02	39.77 ± 0.99

Interestingly, the crystallization temperature (Tc) of 0.5 wt% HEM was lower than that of the other matrices. However, when the concentration of HEM increased to 2 wt%, the Tc returned to the original PP level. Doumeng et al. [59] reported that Tc fluctuated with increasing matrix concentration, which suggests that the decrease in Tc is caused by the matrix hindering grain growth. Therefore, the decrease in Tc at 0.5 wt% concentration is due to the HEM hindering grain growth, resulting in the formation of incomplete crystals.

E. UV Blocking and NIR Emission Characteristics of PP Films with Functional Matrix

The UV-VIS NIR spectra shown in Fig. 8 were obtained to evaluate the UV blocking and NIR emission characteristics of PP films with matrix. The transmittance percentage was used to calculate the UPF. The arithmetic means of UVA, UVB, UVR shielding, and NIR emission are shown in Table 2. A high NIR emission percentage is important to prevent excessive heat accumulation, especially in applications such as textiles and PP surface coatings. Effective NIR emission can reduce indirect skin damage caused by heat while improving thermal comfort. Pure PP had no UV blocking effect, with a UPF of only 7.31 and a UVR_{AV} of only 16.58%. When only 0.5 wt% of GN was added to PVC, the film achieved excellent UV blocking and NIR emission effects, with a UPF value of 58.05, a UVR_{AV} of 2.22%, and a NIR emission of 82.58%. Lijun Qu reported that the enhanced UV protection effect after incorporating graphene was due to the unique 2D planar structure of graphene, which absorbs UV at short wavelengths and reflects UV at long wavelengths [58]. The enhanced NIR emission effect after incorporating GN into the matrix was attributed to the molecular dissipation of incident energy due to color and the presence of numerous sp2-hybridized free electrons [59].

BIOC is also a suitable matrix to be added to PP to improve the UV blocking and NIR emission properties. At a concentration of 0.5 wt%, it can achieve a UPF of 15.79, a UVR_{AV} of 8.42% (considered as good UV protection), and a NIR emittance of 75.09%. Although the UPF value is still lower than that of PP films with HEM and ROCH, when the concentration is increased to 2 wt%, the functionality of PP with BIOC film is improved, reaching a UPF value of 91.41 (UPF 50+, excellent UV blocking), a UVR_{AV} of 1.56%, and a NIR emittance of 95.85%. The absorption of UV/NIR light by carbon materials depends on the island size of sp2 clusters. A larger cluster size can decrease the optical bandgap of UV/NIR absorption, thus increasing the electromagnetic radiation absorption [60]. Marrot et al. [42] reported that pyrolysis of carbonaceous waste at temperatures of at least 600◦C resulted in the presence of defective graphene sp2 clusters. Exposure to UV can cause adverse human health effects such as sunburn, skin aging, and cancer [61]. The UPF achieved by adding 2 wt% BIOC is higher than the UPF of previously reported zinc oxide-based sunscreens [62,63]. Long-term exposure to NIR can cause photoaging [64] and cataracts [65]. The NIR shielding capability of various sunscreens claiming to have NIR-emitting capabilities has not been reported for comparison. A significant reduction in UVA_{AV} and UVB_AV percentages may help prevent sunburn and reduce the risk of skin cancer, respectively [12].
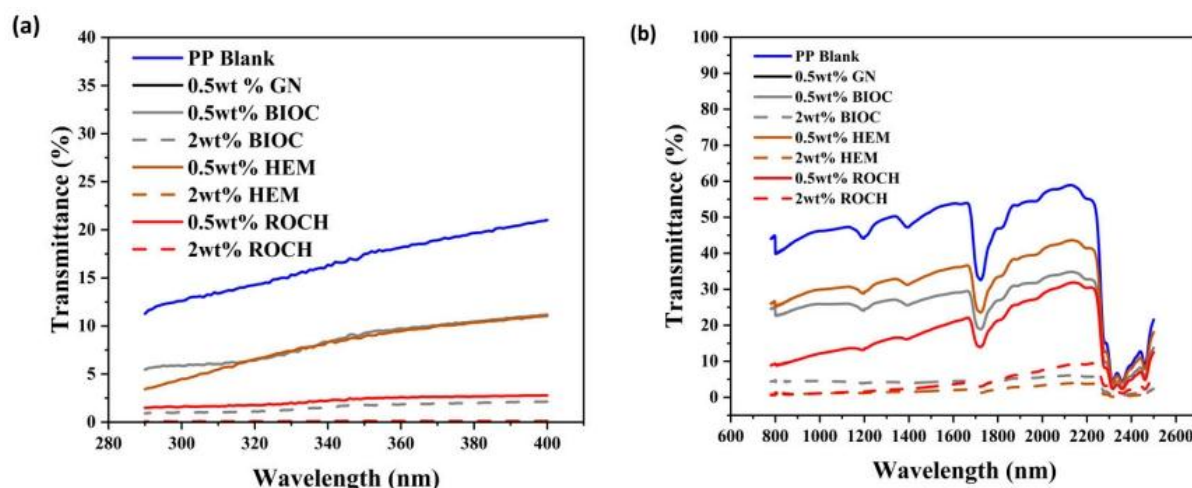
Fig.8. UV-Vis NIR characterization of PP films with matrix: (a) UV spectrum with radiation at 290-400 nm; (b) NIR spectrum with radiation at 780-2500 nm

Table 2. Mean ultraviolet protection factor (UPF), UPF protection category, mean UVA, UVB, ultraviolet radiation (UVR) transmittance, and percentage of NIR shielding of the films with matrixes

Films	UPF	UPF Protection Category	UVA AV, (%)	UVB AV, (%)	UVR AV, %	NIR Shielding, %
PP BLK	7.31	No protection	17.71	12.74	16.58	56.02
0.5 wt% GN	58.05	Excellent protection	2.40	1.61	2.22	82.58
0.5 wt% BIOC	15.79	Good protection	9.14	5.89	8.42	75.09
2 wt% BIOC	91.41	Excellent protection	1.72	1.00	1.56	95.85
0.5 wt% HEM	8.03	No protection	9.03	4.72	17.73	69.59
2 wt% HEM	1142.38	Excellent protection	0.11	0.08	0.11	98.19
0.5 wt% ROCH	58.05	Excellent protection	2.40	1.61	2.22	82.58
2 wt% ROCH	2529.36	Excellent protection	0.06	0.04	0.05	96.31

F. Mechanical properties of PP films with added functional matrix

The mechanical properties of pristine PP films and films with additives are shown in Table 3.

The mechanical properties of pure PP films and films with matrix are shown in Table 3. The tensile stress and elongation at break of pure PP films were 30 MPa and 4.22%, respectively, which are consistent with the results reported by H. Bhunia [66]. In general, all PP samples with added matrix exhibited higher Young's modulus. In terms of tensile strength, the ultimate tensile stress (UTS) and elongation at break of PP films significantly decreased when GN, HEM, and ROCH were added compared to pure PP films. The decrease in UTS and elongation at break may be due to the stress concentration caused by the weak bonding between the PP matrix and these iron oxide-based additives, since iron oxide has much higher surface energy than PP [67]. In addition, mixing inorganic fillers can hinder the movement of PP chains, thereby limiting the deformation and energy absorption of PP [68]. GN is prone to agglomeration. This may reduce the dispersion of graphene within the PP matrix, which may deteriorate the mechanical properties of the composites.

Conversely, incorporation of BIOC into PP results in no change in UTS and only a slight decrease in elongation at break compared to pure PP even when the concentration is increased from 0.5 to 2 wt%. GN exhibits a higher degree of graphitization and is expected to have better mechanical properties based on the results of Raman spectroscopy. However, the presence of functional groups in the matrix which can form a robust polymer–filler interface is an important factor in achieving improved mechanical properties. The pyrolysis temperature of 600◦C in the presence of AC cannot completely remove polar functional groups such as C–O, C=O, COOH, and OH, thereby reducing the polymer–filler bonding interactions with non-polar polymers like polypropylene [69]. The poor polymer–filler interaction is the cause for a slight decrease in elongation at break compared to pure PP, but it still remains more ductile compared to other mineral-based matrices in PP. Mechanical properties are important in preventing permanent deformation under applied load and repeated use in fiber materials. The satisfactory performance of BIOC in PP in terms of optical, mechanical and efflux properties indicate its potential for use in applications such as health textiles and belts/medical devices. Incorporating BIOC into PP can enable textiles and belts/medical devices to effectively block UV rays while

providing other beneficial properties such as improved thermal regulation, which is expected to help maintain and heal human health.

IV. CONCLUSION

In this study, BIOC, hematite, and red ochre were blended with polypropylene (PP) at 0.5 and 2 wt% and their performance was compared with that of graphene/PP composites at 0.5 wt%. All the matrix additions enhanced the FIR emissivity in the range of 5–14 μm, with the highest value recorded at 0.97 for the composites containing red ochre. Additionally, all the additives in the PP films exhibited excellent UV protection (UPF +50) at 2 wt%, with red ochre achieving the highest protection factor. Furthermore, all the composites provided excellent NIR enhancement.

Furthermore, all the matrices increased the heat storage capacity of the PP films when exposed to FIR irradiance. BIOC exhibited excellent heat capacity, with these films achieving a temperature increase of +48.89C at 2 wt% when exposed to FIR source for 30 s, suggesting a 3.3 times higher increase than pure PP. The potential of BIOCas a warm clothing material is further supported by the lowest heat release rate at 2 wt% concentration, suggesting that it may provide a warmer feel than other matrices.

In addition, BIOCshowed better thermal and mechanical properties than other matrices, as the mechanical properties of PP films did not change significantly when BIOCwas incorporated. Despite these promising results indicating that BIOCis a suitable matrix for applications such as FIR fibers and health belts and medical devices, further studies on fibers and health belts and medical devices incorporating this matrix are needed. The manufacturing processes of yarns and polymer films are different, which may affect the properties investigated in this study.

REFERENCES

[1]. Bontemps, B.; Gruet, M.; Vercruyssen, F.; Louis, J. Utilisation of far infrared-emitting garments for optimising performance and recovery in sport: Real potential or new fad? A systematic review. PLoS ONE 2021, 16, e0251282.
[2]. Hamada, Y.; Teraoka, F.; Matsumoto, T.; Madachi, A.; Toki, F.; Uda, E.; Hase, R.; Takahashi, J.; Matsuura, N. Effect of Far Infrared ray on Jela Cells and WI-38 Cells. Int. Congr. Ser. 2003, 1255, 339–341.
[3]. Dyer, J. Infrared functional textiles. In Functional Textiles for Improved Performance, Protection and Health; Elsevier: Amsterdam, The Netherlands, 2011; 184–197.
[4]. Chang, J.-C.; Wu, S.-L.; Hoel, F.; Cheng, Y.-S.; Liu, K.-H.; Hsieh, M.; Hoel, A.; Tronstad, K.J.; Yan, K.-C.; Hsieh, C.-L.; et al. Far-infrared radiation protects viability in a cell model of Spinocerebellar Ataxia by preventing polyQ protein accumulation and improving mitochondrial function. Sci. Rep. 2016, 6, 30436.
[5]. McCall, W.V.; Letton, A.; Lundeen, J.; Case, D.; Cidral-Filho, F.J. The effect of far-infrared emitting sheets on sleep. Res. J. Text. Appar. 2018, 22, 247–259.
[6]. Worobets, J.T.; Skolnik, E.R.; Stefanyshyn, D.J. Apparel with Far Infrared Radiation for Decreasing an Athlete's Oxygen Consumption during Submaximal Exercise. Res. J. Text. Appar. 2015, 19, 52–57.
[7]. Liu, J.; Meng, J.; Liang, J.; Huo, X. Effect of far infrared radiation ceramics containing rare earth additives on surface tension of water. J. Rare Earths 2014, 32, 890–894.
[8]. Gao, Z.; Liang, J.; Zhang, H.; Meng, J. Strengthening mechanism of far-infrared radiation of tourmaline in iron-tailing ceramics. Ceram. Int. 2021, 47, 25214–25220.
[9]. He, P.; Low, R.J.Y.; Burns, S.F.; Lipik, V.; Tok, A.I.Y. Enhanced far infrared emissivity, UV protection and near-infrared shielding of polypropylene composites via incorporation of natural mineral for functional fabric development. Sci. Rep. 2023, 13, 22329.
[10]. Matsumoto, T.; Koizumi, T.; Kawakami, Y.; Okamoto, K.; Tomita, M. Perfect blackbody radiation from a graphene nanostructure with application to high-temperature spectral emissivity measurements. Opt. Express 2013, 21, 30964.
[11]. Zhao, X.; Zhang, Y.; Xu, J.; Chen, D.; Chen, G. The synergistic effects study between metal oxides and graphene on far-infrared emission performance. SN Appl. Sci. 2020, 2, 610.
[12]. Hoang-Minh, T.; Le, T.L.; Kasbohm, J.; Gieré, R. UV-protection characteristics of some clays. Appl. Clay Sci. 2010, 48, 349–357.
[13]. Ouadil, B.; Cherkaoui, O.; Safi, M.; Zahouily, M. Surface modification of knit polyester fabric for mechanical, electrical and UV protection properties by coating with graphene oxide, graphene and graphene/silver nanocomposites. Appl. Surf. Sci. 2017, 414, 292–302.
[14]. Kim, H.S.; Bae, H.S.; Yu, J.; Kim, S.Y. Thermal conductivity of polymer composites with the geometrical characteristics of graphene nanoplatelets. Sci. Rep. 2016, 6, 26825.
[15]. Rufus, A.; Sreeju, N.; Philip, D. Synthesis of biogenic hematite (α-Fe2O3) nanoparticles for antibacterial and nanofluid applications. RSC Adv. 2016, 6, 94206–94217.
[16]. Shahrousvand, M.; Hoseinian, M.S.; Ghollasi, M.; Karbalaeimahdi, A.; Salimi, A.; Tabar, F.A. Flexible magnetic polyurethane/Fe2O3 nanoparticles as organic-inorganic nanocomposites for biomedical applications: Properties and cell behavior. Mater. Sci. Eng. C 2017, 74, 556–567.
[17]. Chaharmahali, M.; Hamzeh, Y.; Ebrahimi, G.; Ashori, A.; Ghasemi, I. Effects of nano-graphene on the physico-mechanical properties of bagasse/polypropylene composites. Polym. Bull. 2014, 71, 337–349.

[18]. Xie, Y.; Hill, C.A.S.; Xiao, Z.; Militz, H.; Mai, C. Silane coupling agents used for natural fiber/polymer composites: A review. Compos. Part Appl. Sci. Manuf. 2010, 41, 806–819.

[19]. Chen, R.; Yu, R.; Pei, X.; Wang, W.; Li, D.; Xu, Z.; Luo, S.; Tang, Y.; Deng, H. Interface design of carbon filler/polymer composites for electromagnetic interference shielding. New J. Chem. 2021, 45, 8370–8385.

[20]. Tang, L.-C.; ZhaoLi, Z.; Qiang, F.; Wu, Q.; Gong, L.-X.; Peng, J.-P. Carbon-Based Nanofillers and Their Rubber Nanocomposites; Elsevier: Amsterdam, The Netherlands, 2019.

[21]. Sae-oui, P.; Sirisinha, C.; Thepsuwan, U.; Hatthapanit, K. Roles of silane coupling agents on properties of silica-filled polychloroprene. Eur. Polym. J. 2006, 42, 479–486.

[22]. Yoo, T.W.; Yoon, H.G.; Choi, S.J.; Kim, M.S.; Kim, Y.H.; Kim, W.N. Effects of compatibilizers on the mechanical properties and interfacial tension of polypropylene and poly(lactic acid) blends. Macromol. Res. 2010, 18, 583–588.

[23]. Kim, D.M.; Lee, H.K; Kwon, Y.S. Graphene health belt with built-in near-infrared LED. Korea Patent 10-2024-0123667. 2024.

[24]. Chang, B.P.; Gupta, A.; Muthuraj, R.; Mekonnen, T.H. Bioresourced fillers for rubber composite sustainability: Current development and future opportunities. Green Chem. 2021, 23, 5337–5378.

[25]. De Gortari, M.G.; Rodriguez-Uribe, A.; Misra, M.; Mohanty, A.K. Insights on the structure-performance relationship of polyphthalamide (PPA) composites reinforced with high-temperature produced biocarbon. RSC Adv. 2020, 10, 26917–26927.

[26]. Kim, D.M.; Lee, G.D. Introduction to the technology, applications, products, Markets R&D, and perspectives of nanofoods in the food industry. J. Food Sci. Nutr. 2006, 11, 348-357.

[27]. Kim, D.M.; Cho, G.S. Nanofood and its materials as Nutrient Delivery System (NDS). Agric. Chem. Biotechnol. 2006, 49(2), 39-47.

[28]. Kim, D.M. Preparation of smart probiotic solid lipid nanoparticles (SLN) for target controlled nanofood. J. Kor. Dairy Sci. Technol. 2007, 25(2), 5-10.

[29]. AS/NZS 4399:1996; Sun Protective Clothing: Evaluation and Classification. Council of Standards Australia: Homebush, NSW, Australia; Council of Standards New Zealand: Wellington, New Zealand, 1996.

[30]. Plastics—Differential Scanning Calorimetry (DSC)—Part 1: General Principles. Available online: https://www.iso.org/obp/ui/#iso:std:iso:11357:-1:ed-4:v1:en (accessed on 12 August 2024).

[31]. Brzozowska-Stanuch, A.; Rabiej, S.; Fabia, J.; Nowak, J. Changes in thermal properties of isotactic polypropyene with different additives during aging process. Polymery 2014, 59, 302–307.

[32]. Standard Test Method for Tensile Properties of Thin Plastic Sheeting. Available online: https://www.astm.org/standards/d882 (accessed on 12 August 2024).

[33]. Pusceddu, E.; Montanaro, A.; Fioravanti, G.; Santilli, S.F.; Foscolo, P.U.; Criscuoli, I.; Raschi, A.; Miglietta, F. A Study on The Recalcitrance of Carbonaceous Structures During Soil Incubation. Int. J. New Technol. Res. 2017, 3, 39–46.

[34]. González-Hourcade, M.; dos Reis, G.S.; Grimm, A.; Dinh, V.M.; Lima, E.C.; Larsson, S.H.; Gentili, F.G. Microalgae biomass as a sustainable precursor to produce nitrogen-doped biochar for efficient removal of emerging pollutants from aqueous media. J. Clean. Prod. 2022, 348, 131280.

[35]. Seto, C.; Chang, B.P.; Tzoganakis, C.; Mekonnen, T.H. Lignin derived nano-biocarbon and its deposition on polyurethane foam for wastewater dye adsorption. Int. J. Biol. Macromol. 2021, 185, 629–643.

[36]. Yan, Y.; Manickam, S.; Lester, E.; Wu, T.; Pang, C.H. Synthesis of graphene oxide and graphene quantum dots from miscanthus via ultrasound-assisted mechano-chemical cracking method. Ultrason. Sonochem. 2021, 73, 105519.

[37]. Ji, R.; Wu, Y.; Bian, Y.; Song, Y.; Sun, Q.; Jiang, X.; Zhang, L.; Han, J.; Cheng, H. Nitrogen-doped porous biomaterial derived from marine algae for efficient solid-phase microextraction of chlorobenzenes from aqueous solution. J. Hazard. Mater. 2021, 407, 124785.

[38]. Gopanna, A.; Mandapati, R.N.; Thomas, S.P.; Rajan, K.; Chavali, M. Fourier transform infrared spectroscopy (FTIR), Raman spectroscopy and wide-angle X-ray scattering (WAXS) of polypropylene (PP)/cyclic olefin copolymer (COC) blends for qualitative and quantitative analysis. Polym. Bull. 2019, 76, 4259–4274.

[39]. Prabowo, I.; Pratama, J.N.; Chalid, M. The effect of modified ijuk fibers to crystallinity of polypropylene composite. In IOP Conference Series: Materials Science and Engineering; IOP Publishing: Bristol, UK, 2017; Volume 223, 12020.

[40]. Caban, R. FTIR-ATR spectroscopic, thermal and microstructural studies on polypropylene-glass fiber composites. J. Mol. Struct. 2022, 1264, 133181.

[41]. Chaiyakun, S.; Witit-Anun, N.; Nuntawong, N.; Chindaudom, P.; Oaew, S.; Kedkeaw, C.; Limsuwan, P. Preparation and characterization of graphene oxide nanosheets. Procedia Eng. 2012, 32, 759–764.

[42]. Marrot, L.; Zouari, M.; Schwarzkopf, M.; DeVallance, D.B. Sustainable carbon/tung oil coatings with hydrophobic and UV-shielding properties for outdoor wood substrates. Prog. Org. Coat. 2023, 177, 107428.

[43]. Mishra, R.K.; Misra, M.; Mohanty, A.K. Value-added biocarbon production through slow pyrolysis of mixed bio-oil wastes: Studies on their physicochemical characteristics and structure–property–processing co-relation. Biomass Conv. Biorefin. 2022, 14, 7887–7901.

[44]. Chamritski, I.; Burns, G. Infrared- and Raman-Active Phonons of Magnetite, Maghemite, and Hematite: A Computer Simulation and Spectroscopic Study. J. Phys. Chem. B 2005, 109, 4965–4968.

[45]. Hu, X.; Tian, M.; Qu, L.; Zhu, S.; Han, G. Multifunctional cotton fabrics with graphene/polyurethane coatings with far-infrared emission, electrical conductivity, and ultraviolet-blocking properties. Carbon 2015, 95, 625–633.

[46]. Huang, J.; Li, Y.; Song, G.; Zhang, X.; Sun, Y.; He, X.; Du, S. Highly enhanced infrared spectral emissivity of porous CeO2 coating. Mater. Lett. 2012, 85, 57–60.

[47]. Xiong, Y.; Huang, S.; Wang, W.; Liu, X.; Li, H. Properties and Applications of High Emissivity Composite Films Based on Far-Infrared Ceramic Powder. Materials 2017, 10, 1370.

[48]. Cottrill, A.L.; Liu, A.T.; Kunai, Y.; Koman, V.B.; Kaplan, A.; Mahajan, S.G.; Liu, P.; Toland, A.R.; Strano, M.S. Ultra-high thermal effusivity materials for resonant ambient thermal energy harvesting. Nat. Commun. 2018, 9, 664.

[49]. Xu, X.; Shen, Y.; Yang, P. Building efficient thermal transport at graphene/polypropylene interfaces by non-covalent functionalized graphene. Phys. Lett. A 2023, 469, 128766.

[50]. Chi, Q.; Ma, T.; Dong, J.; Cui, Y.; Zhang, Y.; Zhang, C.; Xu, S.; Wang, X.; Lei, Q. Enhanced Thermal Conductivity and Dielectric Properties of Iron Oxide/Polyethylene Nanocomposites Induced by a Magnetic Field. Sci. Rep. 2017, 7, 3072.

[51]. Bordoloi, U.; Das, D.; Kashyap, D.; Patwa, D.; Bora, P.; Muigai, H.H.; Kalita, P. Synthesis and comparative analysis of biochar based form-stable phase change materials for thermal management of buildings. J. Energy Storage 2022, 55, 105801.

[52]. Sankauskaite, A.; Rubežiene, V.; Kubiliene, D.; Abraitiene, A.; Baltušnikaite-Guzaitiene, J.; Dubinskaite, K. Investigation of Thermal Behavior of 3D PET Knits with Different Bioceramic Additives. Polymers 2020, 12, 1319.

[53]. Mak, K.F.; Ju, L.; Wang, F.; Heinz, T.F. Optical spectroscopy of graphene: From the far infrared to the ultraviolet. Solid State Commun. 2012, 152, 1341–1349.

[54]. Jeon, J.; Park, J.H.; Wi, S.; Yang, S.; Ok, Y.S.; Kim, S. Characterization of biocomposite using coconut oil impregnated biochar as latent heat storage insulation. Chemosphere 2019, 236, 124269.

[55]. Das, O.; Bhattacharyya, D.; Hui, D.; Lau, K.-T. Mechanical and flammability characterisations of biochar/polypropylene biocomposites. Compos. Part B Eng. 2016, 106, 120–128.

[56]. Piffer, V.S.; Soares, K.; Galdino, A.G.S. Evaluation of mechanical and thermal properties of PP/iron ore tailing composites. Compos. Part B Eng. 2021, 221, 109001.

[57]. Doumeng, M.; Berthet, F.; Delbé, K.; Marsan, O.; Denape, J.; Chabert, F. Effect of size, concentration, and nature of fillers on crystallinity, thermal, and mechanical properties of polyetheretherketone composites. J. Appl. Polym. Sci. 2022, 139, 51574.

[58]. Qu, L.; Tian, M.; Hu, X.; Wang, Y.; Zhu, S.; Guo, X.; Han, G.; Zhang, X.; Sun, K.; Tang, X. Functionalization of cotton fabric at low graphene nanoplate content for ultrastrong ultraviolet blocking. Carbon 2014, 80, 565–574.

[59]. Bramhecha, I.; Sheikh, J. Antibacterial and waterproof breathable waterborne polyurethane functionalised by graphene to develop UV and NIR-protective cotton fabric. Carbon Trends 2021, 4, 100067.

[60]. Bond, T.C.; Bergstrom, R.W. Light Absorption by Carbonaceous Particles: An Investigative Review. Aerosol Sci. Technol. 2006, 40, 27–67.

[61]. Kibria, G.; Repon, R.; Hossain, F.; Islam, T.; Jalil, M.A.; Aljabri, M.D.; Rahman, M.M. UV-blocking cotton fabric design for comfortable summer wears: Factors, durability and nanomaterials. Cellulose 2022, 29, 7555–7585.

[62]. Beasley, D.G.; Meyer, T.A. Characterization of the UVA Protection Provided by Avobenzone, Zinc Oxide, and Titanium Dioxide in Broad-Spectrum Sunscreen Products. Am. J. Clin. Dermatol. 2010, 11, 413–421.

[63]. Zhang, Z.; Wang, Y.; Li, T.; Wu, J.; Huang, J.; Jiang, J.; Chen, M.; Dong, W. Mussel-inspired anti-permeation hybrid sunscreen with reinforced UV-blocking and safety performance. Colloids Surf. Physicochem. Eng. Asp. 2023, 676, 132140.

[64]. Schroeder, P.; Haendeler, J.; Krutmann, J. The role of near infrared radiation in photoaging of the skin. Exp. Gerontol. 2008, 43, 629–632.

[65]. Okuno, T.; Kojima, M.; Yamaguchi-Sekino, S.; Ishiba, Y.; Suzuki, Y.; Sliney, D.H. Cataract Formation by Near-infrared Radiation in Rabbits. Photochem. Photobiol. 2021, 97, 372–376.

[66]. Sable, S.; Ahuja, S.; Bhunia, H. Preparation and Characterization of Oxo-degradable Polypropylene Composites Containing a Modified Pro-oxidant. J. Polym. Environ. 2021, 29, 721–733.

[67]. Guo, Z.; Lei, K.; Li, Y.; Ng, H.W.; Prikhodko, S.; Hahn, H.T. Fabrication and characterization of iron oxide nanoparticles reinforced vinyl-ester resin nanocomposites. Compos. Sci. Technol. 2008, 68, 1513–1520.

[68]. Nurdina, A.K.; Mariatti, M.; Samayamutthirian, P. Effect of single-mineral filler and hybrid-mineral filler additives on the properties of polypropylene composites. J. Vinyl Addit. Technol. 2009, 15, 20–28.

[69]. Drupitha, M.P.; Misra, M.; Mohanty, A.K. Recent advances on value-added biocarbon preparation by the pyrolysis of renewable and waste biomass, their structure and properties: A move toward an ecofriendly alternative to carbon black. Environ. Sci. Adv. 2023, 2, 1282–1301.